

# Magnetic Ordering in Moiré Graphene Multilayers from a Continuum Hartree+U Approach

Christopher T. S. Cheung,<sup>1</sup> Valerio Vitale,<sup>1, 2, 3</sup> Lennart Klebl,<sup>4</sup> Ammon Fischer,<sup>5, 6</sup> Dante M. Kennes,<sup>5, 6</sup> Arash A. Mostofi,<sup>1</sup> Johannes Lischner,<sup>1</sup> and Zachary A. H. Goodwin<sup>1, 7, 8</sup>

<sup>1</sup>*Departments of Physics and Materials and the Thomas Young center for Theory and Simulation of Materials, Imperial College London, South Kensington Campus, London SW7 2AZ, UK*

<sup>2</sup>*Dipartimento di Fisica, Università degli Studi di Trieste, strada costiera 11, 34151 Trieste, Italy*

<sup>3</sup>*CNR-IOM-Istituto Officina dei Materiali, National Research Council of Italy, c/o SISSA Via Bonomea 265, Trieste IT-34136, Italy*

<sup>4</sup>*Institut für Theoretische Physik und Astrophysik and Würzburg-Dresden Cluster of Excellence ct.qmat, Universität Würzburg, 97074 Würzburg, Germany*

<sup>5</sup>*Max Planck Institute for the Structure and Dynamics of Matter, Center for Free Electron Laser Science, 22761 Hamburg, Germany*

<sup>6</sup>*Institute for Theory of Statistical Physics, RWTH Aachen University, and JARA Fundamentals of Future Information Technology, 52062 Aachen, Germany*

<sup>7</sup>*John A. Paulson School of Engineering and Applied Sciences, Harvard University, Cambridge, MA 02138, USA*

<sup>8</sup>*Department of Materials, University of Oxford, Parks Road, Oxford OX1 3PH, United Kingdom*

(Dated: September 24, 2025)

Recently, symmetry-broken ground states, such as correlated insulating states, magnetic order and superconductivity, have been discovered in twisted bilayer graphene (tBLG) and twisted trilayer graphene (tTLG) near the so-called magic-angle. Understanding the magnetic order in these systems is challenging, as atomistic methods become extremely expensive near the magic angle and continuum approaches fail to capture important atomistic details. In this work, we develop a self-consistent approach based on a continuum model that incorporates both short-ranged Hubbard interactions and long-ranged Coulomb interactions, therefore allowing efficient exploration of magnetic order in moiré graphene multilayers. With this approach, we perform a systematic analysis of the magnetic phase diagram of tBLG as a function of doping level and twist angle, near the magic angle. We find that the results are consistent with previous perturbative atomistic Hartree+U calculations. Furthermore, we predict stable magnetic orders for the tTLG. We found that the magnetic orders are similar to those in tBLG for small values of on-site repulsion. In the future, the developed method can be utilized to investigate magnetic ordering tendencies from short-range exchange interactions in other moiré graphene multilayers as a function of doping, twist angle, screening environment, among other variables.

## I. INTRODUCTION

Since the discovery of correlated insulating states<sup>1</sup> and superconductivity<sup>2</sup> in magic-angle twisted bilayer graphene (tBLG), moiré materials have emerged as an excellent platform for understanding flat-band physics and strongly-correlated electrons. This is demonstrated by the unprecedented variety of exotic electronic states that have been experimentally observed in tBLG, such as global charge-ordered stripe phases<sup>3</sup>, ferromagnetic chiral edge states<sup>4</sup>, orbital magnetism<sup>5</sup>, amongst other experimental and theoretical findings<sup>3, 5–35</sup>. After these discoveries, flat-band physics and strong correlations have been discovered in moiré materials other than tBLG. For example, still using graphene as a building block, twisted trilayer graphene<sup>36, 37</sup> (tTLG), twisted double bilayer graphene (tDBLG)<sup>38–41</sup>, among other systems<sup>42</sup> have been actively investigated, and correlated insulating states and superconductivity have been found in these systems as well. Also, multilayer graphene systems without a twist have been revisited; for example, superconductivity and magnetism have been discovered in rhombohedral graphene multilayers<sup>43–49</sup>. In addition

to twisted graphitic materials, twisted bilayers and multilayers consisting of other 2D materials have also been investigated, such as semiconducting transition metal dichalcogenides (TMDs)<sup>50–52</sup>, such as superconductivity in tWSe<sub>2</sub><sup>53, 54</sup> and fractional states in MoTe<sub>2</sub><sup>55</sup>, or metallic TMDs<sup>56, 57</sup>, hexagonal boron nitride<sup>58, 59</sup>, among other examples<sup>30</sup>.

In tBLG, the existence of flat bands near the Fermi energy at specific twist angles, referred to as magic angles, was predicted by a continuum model proposed by Bistritzer and MacDonald<sup>60</sup>. Theoretical effort has since been mainly devoted to incorporating interactions into the electronic Hamiltonian of this continuum model. Notably, Guinea *et al.* incorporated long-ranged Hartree interactions into the continuum model, predicting strong distortions of the flat bands near the magic angle<sup>61–64</sup>. Long-ranged exchange, i.e. Fock, interactions have also been included in the continuum model, giving rise to various broken symmetry states in reasonable agreement with experimental measurements<sup>63–65</sup>. Whereas these models are based on the reciprocal space continuum model, alternative approaches, based on the Wannier functions of the flat bands, have also had successes in

explaining experimental measurements<sup>10,66–70</sup>. However, neither of these techniques has clearly determined the role of short-ranged interactions, as separating the effects of short-range and long-range interactions in these methods is difficult.

Atomistic models, on the other hand, can naturally include short-ranged interactions, such as the onsite repulsion between electrons in the  $p_z$  orbitals<sup>71–74</sup>. The magnetic phases of tBLG have been studied using perturbative random phase approximation (RPA) atomistic calculations at the magic angle by Klebl *et al.*<sup>75–77</sup>, which predicted the existence of emergent moiré-scale modulated antiferromagnetic and ferromagnetic states<sup>75</sup>. Klebl *et al.*<sup>75,76</sup> have also mapped the magnetic phase diagram of tBLG over a larger range of twist angles at all doping levels up to  $\pm 3$  electrons per moiré unit cell taking into account long-ranged Hartree interactions (in a perturbative way)<sup>76</sup>. However, a major challenge presented by atomistic tight-binding approaches is the computational cost of reaching converged solutions for small twist-angle systems<sup>71–74</sup>, which has typically limited the work to perturbative calculations. Motivated by the low computational cost of continuum models, and the success of atomistic models in capturing short-ranged interactions, Jimeno-Pozo *et al.*<sup>78</sup> developed a hybrid approach to incorporate Hubbard interactions into the continuum method based on atomistic results<sup>75,76</sup>. The magnetic orders predicted by the atomistic models were incorporated into the continuum model through a sublattice-polarized moiré expansion with order parameters that need to be determined, similar to how Hartree interactions are included in the continuum model<sup>78</sup>. Inspection of the band structures obtained from constrained Hartree-Fock+U calculations for various magnetic orders has led to the prediction that some of the symmetry-broken phases are favoured by the long-ranged Hartree-Fock potential. Those calculations, however, were only perturbative.

In this work, we develop and perform self-consistent Hartree+U calculations in the continuum model of moiré graphene multilayers. Using this methodology, we compute the self-consistent order parameters of possible magnetic instabilities, giving us insight into the regions of stability for each competing magnetic ground state in tBLG, over a range of doping levels in the flat bands and a range of twist angles near the magic angle. The approach is general, which we demonstrate by also predicting self-consistently determined quasiparticle band structures for twisted symmetric trilayer graphene (tTLG), with a mirror symmetry with respect to the middle layer, at the magic angle of  $1.54^\circ$  in different possible magnetic orders, where we found similarities to tBLG. We hope that this method will open up avenues that can include both short and long range exchange interactions, to determine their relative importance. Moreover, the developed method could also be used for other moiré graphene multilayers, or moiré systems comprising other 2D materials.

## II. METHODS

The approach we take here is a combination of atomistic and continuum models. First, we determine the leading magnetic instabilities using an RPA theory based on the atomistic tight-binding model. As these magnetic instabilities have already been discussed in depth elsewhere, we refer the reader to Refs.<sup>75,76</sup> for the details of these calculations. These leading magnetic instabilities are then included in the continuum model by approximating their form with a sum of trigonometric functions. The reader should refer to Ref.<sup>78</sup> for a more detailed description of this procedure. In the remainder of the Methods section, we outline the self-consistent continuum model approach developed here, which builds on the previously mentioned work.

### A. Continuum model for tBLG

The atomic structure of tBLG is obtained by rotating the top and bottom layers by  $\pm\theta/2$ , where  $\theta$  is the twist angle. As we build on atomistic methods, we choose commensurate twist angle moiré unit cells, described by the moiré lattice vector  $\mathbf{R}_1 = m\mathbf{a}_1 + n\mathbf{a}_2$ , with  $(m, n)$  being non-equal integers, and  $\mathbf{a}_1 = (\sqrt{3}/2, -1/2)a_0$ ,  $\mathbf{a}_2 = (\sqrt{3}/2, 1/2)a_0$  are the graphene unit cell vectors. The lattice constant  $a_0$  is taken as  $2.46 \text{ \AA}$ .

The low-energy electronic properties of tBLG without any electron-electron interactions are described with a Bistritzer-MacDonald continuum model<sup>60</sup> as

$$\mathcal{H}^x(\mathbf{k}) = \begin{pmatrix} \mathcal{H}^{1,x}(\mathbf{k}) & \mathcal{U}^{x,\dagger} \\ \mathcal{U}^x & \mathcal{H}^{2,x}(\mathbf{k}) \end{pmatrix}, \quad (1)$$

where  $\mathcal{H}^{l,x}(\mathbf{k})$  is the  $l$ -th intralayer Dirac Hamiltonian for layer  $l \in \{1, 2\}$  and valley  $x$  [ $x$  is taken as  $1(-1)$  for the  $K(K')$ -valley]. For the  $l$ -th intralayer Dirac Hamiltonian, we expand it in the moiré reciprocal lattice vectors. Hence, the  $(N, M)$ -th entry of Eq. (1) is a  $2 \times 2$  submatrix describing the sublattice coupling as

$$\mathcal{H}_{N,M}^{l,x}(\mathbf{k}) = \begin{pmatrix} 0 & h^{l,x}(\mathbf{k} + \mathbf{G}_{N,M}) \\ h^{l,x}(\mathbf{k} + \mathbf{G}_{N,M}) & 0 \end{pmatrix}, \quad (2)$$

where  $\mathbf{G}_{N,M}$  is a moiré reciprocal lattice vector given by  $\mathbf{G}_{N,M} = N\mathbf{G}_1 + M\mathbf{G}_2$ , with  $\mathbf{G}_1 = 2\pi/L(1/\sqrt{3}, 1)$  and  $\mathbf{G}_2 = 4\pi/L(-1/\sqrt{3}, 0)$ , where  $L$  is the length of the moiré cell vectors. The integers  $N, M$  run over the set  $\mathcal{M}$  that indexes moiré reciprocal lattice vectors such that they satisfy

$$\mathcal{M} = \{(N, M) \in \mathbb{Z}^2 \mid \|\mathbf{G}_{N,M}\| \leq p_{\max} \|\mathbf{G}_1\|\}. \quad (3)$$

Here  $p_{\max}$  is an integer controlling the cutoff radius in reciprocal space, and was taken as 5.

The functions  $h^{l,x}(\mathbf{q})$  are given by

$$h^{l,x}(\mathbf{q}) = \chi \hbar v_F (\mathbf{q} - \chi \mathbf{K}_l) \cdot \boldsymbol{\tau}_{\theta,l}^x, \quad (4)$$

where  $\mathbf{K}_l$  is the Dirac point associated with the  $l$ -th layer,  $v_F = \sqrt{3}ta_0/2\hbar$  is the Fermi velocity in graphene, with  $t$  the hopping amplitude between localized  $p_z$  orbitals, and

$$\tau_{\theta,l}^\chi = \exp(i\chi\tau_z\theta_l/2)(\tau_x, \chi\tau_y) \exp(-i\chi\tau_z\theta_l/2), \quad (5)$$

with  $\tau_i$  being the corresponding Pauli matrices, and  $\theta_{1,2} = \mp\theta/2$ .

Moving on to the interlayer Hamiltonians, we adopt the interlayer coupling for  $\mathcal{U}$ <sup>62–64</sup>, with the  $(N, M)$ -th submatrix given by

$$\begin{aligned} \mathcal{U}_{N,M}^\chi = & U_1^\chi \delta^{(2)}(\mathbf{G}_N - \mathbf{G}_M) + \\ & U_2^\chi \delta^{(2)}(\mathbf{G}_N - \mathbf{G}_M - \chi\mathbf{G}_1) + \\ & U_3^\chi \delta^{(2)}(\mathbf{G}_N - \mathbf{G}_M - \chi(\mathbf{G}_1 + \mathbf{G}_2)), \end{aligned} \quad (6)$$

with

$$\begin{aligned} U_1^\chi &= \begin{pmatrix} u_1 & u_2 \\ u_2 & u_1 \end{pmatrix} \\ U_2^\chi &= \begin{pmatrix} u_1 & u_2 \exp(-i\frac{2\pi\chi}{3}) \\ u_2 \exp(i\frac{2\pi\chi}{3}) & u_1 \end{pmatrix} \\ U_3^\chi &= \begin{pmatrix} u_1 & u_2 \exp(i\frac{2\pi\chi}{3}) \\ u_2 \exp(-i\frac{2\pi\chi}{3}) & u_1 \end{pmatrix}, \end{aligned} \quad (7)$$

acting on the sublattice subspace. The interlayer tunnelings  $u_{1,2}$  are taken as  $u_1 = 0.0797$  eV and  $u_2 = 0.0975$  eV<sup>67,79</sup>. Here  $\delta^{(2)}$  is a Kronecker delta function acting in the 2D reciprocal space.

For the Hartree electron-electron interactions, we adopt the description proposed by Guinea *et al.*<sup>61</sup>, where the Hartree Hamiltonian submatrix is given by

$$\mathcal{H}^H = \frac{\delta\rho_G}{\epsilon L} \mathbb{1}, \quad (8)$$

where  $\epsilon$  is the effective dielectric constant describing the external and internal screening from the environment and electrons, which is taken as  $\epsilon = 24$  in the calculations<sup>80</sup>. The only parameter in this Hamiltonian to be solved self-consistently is  $\delta\rho_G$ , which describes the electronic density localized on the moiré scale.

Following Ref.<sup>78</sup>, the mean-field Hubbard interactions between electrons due to magnetic ordering are captured by the inter-sublattice coupling Hamiltonian

$$\begin{aligned} \mathcal{H}_{N,M}^U = & \delta_0 \mathcal{S} \delta^{(2)}(\mathbf{G}_N - \mathbf{G}_M) + \\ & \delta_1 \mathcal{S} \sum_{\mathbf{G}_\alpha} \delta^{(2)}(\mathbf{G}_N - \mathbf{G}_M - \mathbf{G}_\alpha), \end{aligned} \quad (9)$$

where  $\mathbf{G}_\alpha$  are the first star of reciprocal moiré lattice vectors,  $\mathcal{S}$  is a  $2 \times 2$  sublattice-coupling matrix describing the constant (moiré-scale) part of the magnetic order parameter. The magnetic order parameters,  $\delta_0$  and  $\delta_1$ , are determined through

$$\delta_0 = 2U(n_{0,\uparrow} - n_{0,\downarrow}), \quad (10)$$

where  $U$  is the Hubbard parameter, the factor of 2 accounts for the valley degeneracy and  $n_{0,\sigma}$  is the spin-polarized constant electron density. The moiré part is also a Hubbard term but proportional to the spin-polarization of the moiré-scale electron density given by

$$\delta_1 = 2U(n_{G,\uparrow} - n_{G,\downarrow}). \quad (11)$$

Incorporating the Hartree,  $\mathcal{H}^H$ , and Hubbard,  $\mathcal{H}^U$ , contributions, we obtain the valley- and spin-projected continuum Hamiltonian as

$$H^{\chi,\sigma}(\mathbf{k}) = \mathcal{H}^H + (-1)^\sigma \mathcal{H}^U + \begin{pmatrix} \mathcal{H}^{1,\chi}(\mathbf{k}) & \mathcal{U}^{\chi,\dagger} \\ \mathcal{U}^\chi & \mathcal{H}^{2,\chi}(\mathbf{k}) \end{pmatrix}, \quad (12)$$

where  $\sigma = 0, 1$  for spin up and down electrons, respectively, and the first two terms  $\propto \mathbb{1}$  in layer space. With the Hamiltonian in Eq.(12), we solve the eigenvalue equation in (13)

$$H^{\chi,\sigma}(\mathbf{k}) \mathbf{c}_{\chi,\sigma}(\mathbf{k}) = E_\sigma^\chi(\mathbf{k}) \mathbf{c}_{\chi,\sigma}(\mathbf{k}), \quad (13)$$

where  $\mathbf{c}_{\chi,\sigma}(\mathbf{k})$  is the eigenvector and  $E_\sigma^\chi(\mathbf{k})$  are the energy eigenvalues for a given spin  $\sigma$ .

The order parameter  $\delta\rho_G$ , which describes the localized electronic density on the moiré scale, is computed from the eigenstates using

$$\begin{aligned} \delta\rho_G = & \frac{1}{N_k} \sum_{n_{\text{occ}} \in [E_N, E_f]} \sum_{\mathbf{k}} \\ & \sum_{\mathbf{G}'} \sum_{\chi, \sigma} c_{n,\chi,\sigma}(\mathbf{k} + \mathbf{G}) c_{n,\chi,\sigma}^*(\mathbf{k} + \mathbf{G} + \mathbf{G}'), \end{aligned} \quad (14)$$

where  $n_{\text{occ}}$  denotes the  $n$ -th occupied band between charge neutrality  $E_N$  and the Fermi level  $E_f$ ,  $N_k$  is the number of  $k$ -points sampled in the mini-Brillouin zone, and  $\sigma$  denotes the spin. We note that in actual calculations the sum over valley  $\chi$  is simplified utilizing the valley-degeneracy. Specifically,  $\delta\rho_G$  is obtained for a particular valley and then multiplied by 2.

The spin-polarized electron density  $n_{G,\sigma}$  in (11) is defined similarly to  $\delta\rho_G$  in (14) as

$$\begin{aligned} n_{G,\sigma} = & \sum_{\mathbf{G}'} n_{G,G',\sigma} \\ = & \frac{2}{N_k} \sum_{n_{\text{occ}}} \sum_{\mathbf{k}} \sum_{\mathbf{G}'} c_{n,\sigma}(\mathbf{k} + \mathbf{G}) c_{n,\sigma}^*(\mathbf{k} + \mathbf{G} + \mathbf{G}'), \end{aligned} \quad (15)$$

with the major difference of leaving out the spin summation. The constant spin-polarised density is defined similarly as

$$\begin{aligned} n_{0,\sigma} = & \sum_{\mathbf{G}} \sum_{\mathbf{G}'} n_{G,G',\sigma} \delta_{0,\mathbf{G}'} \\ = & \frac{2}{N_k} \sum_{n_{\text{occ}}} \sum_{\mathbf{k}} \sum_{\mathbf{G}} c_{n,\sigma}(\mathbf{k} + \mathbf{G}) c_{n,\sigma}^*(\mathbf{k} + \mathbf{G}). \end{aligned} \quad (16)$$

We note that in calculating these densities, all bands below the Fermi level are taken into account, in contrast

to the expression for  $\delta\rho_G$  in Eq. (14), and the factor of 2 in these equations comes from a valley degeneracy.

The order parameters  $\delta_0$ ,  $\delta_1$ , and  $\delta\rho_G$  are obtained self-consistently. The convergence criterion was chosen so that the total difference between the successive values of all 3 order parameters is less than  $10^{-6}$ . We note that occasionally the criterion is relaxed for metallic systems. Nonetheless, the parameters are converged to at least 3 significant figures.

The constants  $\delta_{0(1)}$  are the Hubbard potential order parameters describing the strength of the constant part (moiré-scale oscillation) of the Hubbard interactions. The constant part is a Hubbard term proportional to the spin-polarization of the constant electron density background. Their definitions for each magnetic ordering are discussed in the Results Section III.

## B. Continuum model for tTLG

In the case of tTLG, the external layers are twisted symmetrically with respect to the central layer, resulting in a mirror-symmetric system. The lattice vectors and commensurate integers which describe the system remain the same as for tBLG. The spin-valley-projected Hamiltonian for twisted trilayer graphene is similar to that for the single layer with a number of modifications. Starting with the general non-interacting Hamiltonian

$$H_0^{\chi,\sigma}(\mathbf{k}) = \begin{pmatrix} \mathcal{H}^{1,\chi}(\mathbf{k}) & \mathcal{U}^{\chi,\dagger} & 0 \\ \mathcal{U}^\chi & \mathcal{H}^{2,\chi}(\mathbf{k}) & \mathcal{U}^\chi \\ 0 & \mathcal{U}^{\chi,\dagger} & \mathcal{H}^{3,\chi}(\mathbf{k}) \end{pmatrix}, \quad (17)$$

the energy eigenstates are solved numerically using Eq. (13). We note that the third-layer Hamiltonian  $\mathcal{H}^{3,\chi}(\mathbf{k})$  has the same form as  $\mathcal{H}^{1,\chi}(\mathbf{k})$ , which in turn is the same as that for the bilayer. We also kept the inner-(second-)layer Hamiltonian and the interlayer coupling matrices unchanged.

Having defined these parameters, the full spin-valley-polarized Hamiltonian incorporating long-ranged Hartree and short-ranged Hubbard interactions is

$$H^{\chi,\sigma}(\mathbf{k}) = H_0^{\chi,\sigma} + \begin{pmatrix} \mathcal{H}^{H,1} & 0 & 0 \\ 0 & \mathcal{H}^{H,2} & 0 \\ 0 & 0 & \mathcal{H}^{H,3} \end{pmatrix} + \begin{pmatrix} \mathcal{H}^{U,\sigma,o} & 0 & 0 \\ 0 & \mathcal{H}^{U,\sigma,i} & 0 \\ 0 & 0 & \mathcal{H}^{U,\sigma,o} \end{pmatrix}. \quad (18)$$

The order parameters  $\delta_{o,0}, \delta_{o,1}, \delta_{i,0}, \delta_{i,1}, \delta\rho_G$  are solved self-consistently similar to the twisted bilayer.

Obtaining the eigenstates allows us to compute the constant charge density  $\delta\rho_0$ , charge neutrality energy level  $E_N$  and Fermi level  $E_F$ , analogously to the twisted bilayer case. These allow us to include Hartree corrections into the Hamiltonian, using the definition

$$\mathcal{H}^{H,l} = \frac{\delta\rho_G^l}{\epsilon L} \mathbb{1}, \quad (19)$$

in which the moiré-scale electronic charge density is split into three layer-polarized contributions.

To construct the full Hamiltonian, we need to include Hubbard terms. The four magnetic orders obtained from atomistic RPA calculations are each parameterized with 4 Hubbard potential order parameters (see the Appendix for their definitions).

The Hubbard Hamiltonian is given by

$$\mathcal{H}_{N,M}^{U,l} = \delta_{l,0} \mathcal{S} \delta^{(2)}(\mathbf{G}_N - \mathbf{G}_M) + \delta_{l,1} \mathcal{S} \sum_{\mathbf{G}_\alpha} \delta^{(2)}(\mathbf{G}_N - \mathbf{G}_M - \mathbf{G}_\alpha), \quad (20)$$

where  $l \in \{1, 2, 3\}$  denotes the outer and inner layers, and all other symbols have the same meaning as in Eq.(9). Nominally,  $\delta_{3,0/1} = \delta_{1,0/1} = \delta_{o,0/1}$  and  $\delta_{2,0/1} = \delta_{i,0/1}$  for the other orders. Similar to tBLG, details of the exact form of the parameters will be given in the Results section III, and we use the same self-consistency criteria for these calculations.

## III. RESULTS

### A. Twisted Bilayer Graphene

#### 1. Leading Instabilities

By performing atomistic RPA calculations at  $\mathbf{q} = 0$ , the leading magnetic instabilities can be obtained. Details of can be found in the papers by Klebl *et al.*<sup>75,76</sup>. The ferromagnetic order (FM), moiré modulated antiferromagnetic (MAFM), and nodal antiferromagnetic (NAFM) orders were found to be the most prevalent in magic-angle tBLG<sup>75,76</sup>. The eigenvectors for these magnetic instabilities,  $\zeta_i$ , can be seen in Fig. 1, the values of which represent the spin-polarized electron density,  $\zeta \propto (n_\uparrow - n_\downarrow)/(n_\uparrow + n_\downarrow)$  where  $n_{\uparrow\downarrow}$  are the spin densities, that characterize these magnetic orders.

As can be seen in Fig. 1, and discussed in detail in Refs.<sup>75,76</sup>, the FM order is mainly characterized by a spin-polarized electron density peaked in the AA regions, which approximately follows a cosine series that only contains the first reciprocal lattice vectors, in addition to a constant shift. Therefore, as the AA region is taken to be centered at the origin, it is reasonable to approximate this FM order by

$$\zeta_{\text{FM}} = \zeta_0 + \zeta_1 \sum_i \cos(\mathbf{G}_i \cdot \mathbf{r}), \quad (21)$$

where  $\mathbf{G}_i$  are the moiré reciprocal lattice vectors ( $\mathbf{G}_1$ ,  $\mathbf{G}_2$ , and  $\mathbf{G}_1 + \mathbf{G}_2$ ),  $\zeta_0$  is a parameter which characterizes the constant spin-polarized electron density in the moiré unit cell which is the same for each sublattice, and  $\zeta_1$  represents the moiré-scale modulation of the FM order which is the same for each sublattice. Therefore, for the FM instability, the sublattice-coupling matrix  $\mathcal{S}$  is taken

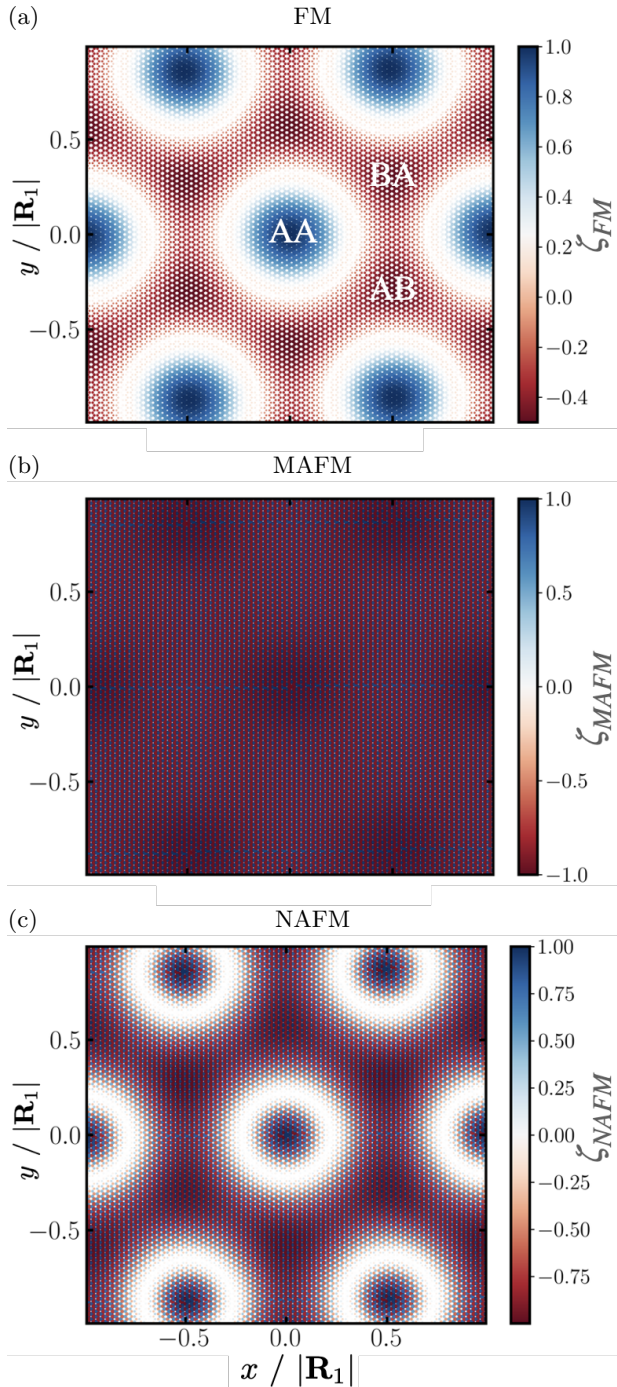


FIG. 1. Magnetic instabilities obtained from atomistic RPA calculations, which are used to incorporate magnetic forms for the continuum model. The ferromagnetic order (FM), moiré modulated antiferromagnetic (MAFM), and nodal antiferromagnetic (NAFM) orders are shown in a), b) and c), respectively. Note these graphs are obtained from the eigenvalues of these calculations, where the largest positive value was chosen to be 1. These values are proportional to the spin-polarised electron density.

to be the identity matrix. For the MAFM order, there is a similar structure to the FM case, but the value of  $\zeta$  changes sign between each sublattice, implying  $\mathcal{S} \propto \sigma_z$ . Therefore, the MAFM order can be approximately characterised by

$$\zeta_{MAFM} = \zeta_0 + \zeta_1 \sum_i \cos(\mathbf{G}_i \mathbf{r}), \quad (22)$$

where  $\zeta_0$  and  $\zeta_1$  have opposite sign for each sublattice, but the same sign within each sublattice on different layers. Finally, the NAFM is analogous to the MAFM case, but without a constant-shift term, which means it can be approximated as

$$\zeta_{NAFM} = \zeta_1 \sum_i \cos(\mathbf{G}_i \mathbf{r}), \quad (23)$$

where again  $\zeta_1$  has the opposite sign for each sublattice, again meaning that  $\mathcal{S}$  is taken as the Pauli matrix  $\sigma_z$ . Following the work of Ref.<sup>78</sup>, these magnetic orders can be incorporated into the continuum model, as shown in the Methods Section II.

## 2. Regions of Stability

Using the leading magnetic instabilities from the atomistic calculations in the previous section, we included these forms in the continuum model and solved the resulting Hamiltonian self-consistently (see Sec. II). To perform these calculations, we need to choose a value of the on-site Hubbard parameter in the continuum model. Following Jimeno-Pozo *et al.*<sup>78</sup>, the Hubbard interaction in tBLG is of the order of 1 meV<sup>61</sup>. We choose  $U = 2$  meV to solve our system of equations self-consistently. To quantify the magnetic order stability, the magnitude of the total order parameter  $|\delta_0| + |\delta_1|$  is displayed, as shown in Fig. 2 as a function of doping level ( $\nu$ ) and twist angle ( $\theta$ ) for the various magnetic ordering tendencies, with and without long-range Coulomb interactions. The cut-off for stability is set at  $|\delta_0| + |\delta_1| \leq 5 \times 10^{-5}$  eV, below which the Hubbard potential order parameters are too weak to induce any observable modifications on the meV scale to the band structures, and therefore the system can reasonably be concluded to be in the normal state.

The total order parameter,  $|\delta_0| + |\delta_1|$ , for MAFM is shown in Fig. 2(a) with account of Hartree interactions. The MAFM magnetic order persists from  $\theta = 1.12^\circ$  to  $\theta = 0.96^\circ$ , but does not exist outside of  $\nu = \pm 2$ . Notably, the symmetry broken state is most strongly stabilized near charge neutrality at  $\theta = 1.08^\circ$ , with a total order parameter of 2.1 meV, away from which, the order parameters are suppressed. Upon doping in the range of  $\theta = 1.08..1.05^\circ$ , stable MAFM order persists up to  $\nu = \pm 2$ , albeit being reduced by an order of magnitude to  $\sim 0.1$  meV at  $\nu = \pm 2$  for  $\theta = 1.08..1.05^\circ$ . For twist angles outside this window, the order parameter decays more rapidly as the system is doped, i.e., more doping

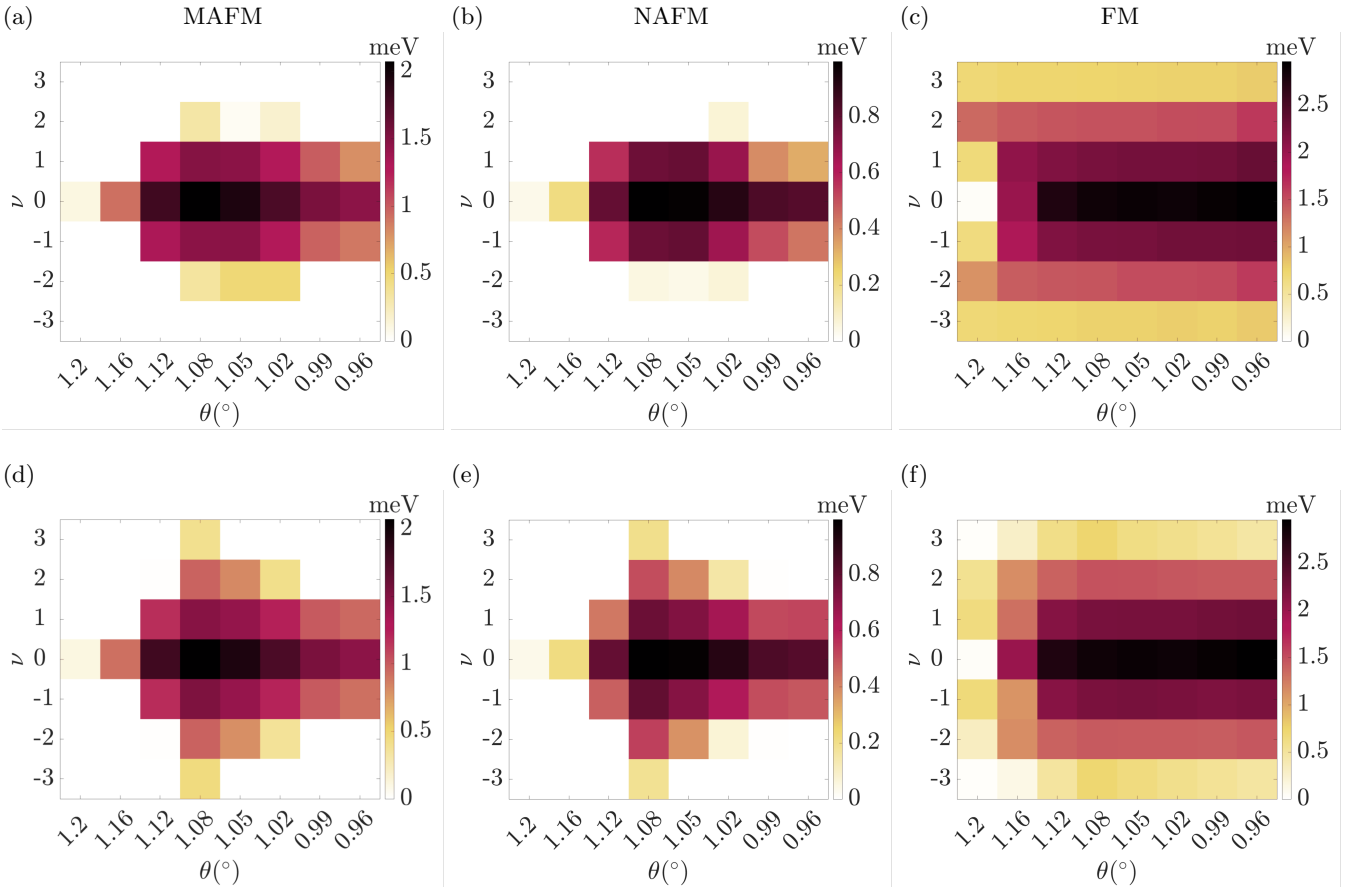


FIG. 2. Magnitudes of Hubbard potential order parameters  $|\delta_0| + |\delta_1|$ , for all the competing magnetic ground states as shown in (a) for MAFM, (b) for NAFM, and (c) for FM with Hartree interactions. Results without Hartree interactions are shown in (d) for MAFM, (e) for NAFM, and (d) for FM.  $U = 2$  meV throughout. We note that  $\delta_0 = 0$  for the NAFM order.

levels near the magic-angle host magnetic order, while the twist angles further from the magic angle only host magnetic order near charge neutrality.

The order parameter for NAFM, as shown in Fig. 2(b), also exhibits a similar variation as function of the twist angle and doping as the MAFM case. The total magnitude at charge neutrality at  $\theta = 1.08^\circ$ , however, is reduced by approximately 1/2, because this order does not have  $\delta_0$ . Again, similar to MAFM, this magnetic order is most stable near charge neutrality at the magic angle.

The FM order shown in Fig. 2(c) is the most stable at charge neutrality, with a total order parameter around 3.5 meV near the magic angle. The FM order is also suppressed upon doping the system, while being constant over twist angles near the magic angle. Upon twisting to larger angles, the magnetic order is suppressed at charge neutrality. At  $\theta = 1.2^\circ$ , the FM order is suppressed at charge neutrality, but stable FM orders are notably developed near  $\nu = \pm 2$ , with a total order parameter amplitude of around 1.4 meV at  $\nu = \pm 2$ . The  $\theta = 1.2^\circ$  twist angle is the only one we observed to have a non-monotonic doping dependence of the FM, whereas for all other angles the FM order parameter decays monotonically from charge neutrality.

The effect of long-ranged interactions is also investigated by considering the value of the magnetic order parameter when the Hartree interactions are not taken into account. In other words, we consider the stability of the magnetic order for different twist angles and doping levels when only short-ranged Hubbard interactions are present. The phase diagrams for these calculations are shown in Figs. 2(d-f).

The antiferromagnetic orders, MAFM [Fig. 2(d)] and NAFM [Fig. 2(e)], have clear differences in the absence of Hartree interactions. The phase diagrams are more electron-hole symmetric compared to when Hartree interactions are taken into account. Furthermore, the magnetic order parameter exists over a wider range of doping levels, and is significant at  $\nu = \pm 3$  of  $\theta = 1.08^\circ$ . Otherwise, the qualitative variations remain similar at other twist angles and dopings.

For the FM order, as shown in Fig. 2(f), the qualitative variation and magnitude of the order parameters are similar to that in the presence of Hartree interaction. However, the reduction of the order parameters is more rapid with doping levels away from charge neutrality, in

contrast to the anti-ferromagnetic order. For example, at  $\theta = 1.16^\circ$ , although the stable orders are still centred around charge neutrality, the magnitude at  $\nu = \pm 3$  is significantly reduced.

Interestingly, comparing Fig. 2(a) and 2(d), and 2(b) and 2(e), we find that the magnetic orders M(N)AFM are enhanced by the long-ranged Hartree interactions at  $\nu = \pm 1$  near the magic angle. Beyond this doping level, Hartree interactions suppress magnetic order. On the contrary, comparing Figure 2(c) and 2(f), the FM order is always enhanced by Hartree interactions. Such differences lie in the interplay between short- and long-ranged interactions, which further underpins the distortions of the band structures.

### 3. Band Structure

The advantage of the approach developed here, unlike the atomistic RPA approach<sup>75</sup> and the perturbative continuum approach<sup>78</sup>, is that self-consistent quasi-particle band structures can also be investigated. In this section, we report these for magic-angle tBLG for the leading instabilities, also as a function of doping with the inclusion of long-range Hartree interactions. We restrict our analysis here to only electron-doped systems, as hole-doping is qualitatively similar (albeit with band distortions in the opposite direction of energy)<sup>81</sup>.

The band structures obtained from the self-consistent calculations at  $\theta = 1.08^\circ$  and  $U = 4$  meV are shown in Fig. 3. The band structures without magnetic order, but with Hartree interactions taken into account (note that when they are not taken into account, it is simply that the  $\nu = 0$  band structure is obtained for all doping levels, as the Hartree interactions in the model at charge neutrality vanish), are shown in Fig. 3(a) for reference. As electrons are added into the normal state of tBLG, this causes the K-points to increase in energy relative to the  $\Gamma$ -points, causing a sensitive dependence of the band structure on doping, and a pinning of the van Hove singularities. At the magic angle, this causes the bands to become more dispersive, but at other twist angles these distortions cause doping-induced band flattening, in addition to the twist-angle induced band flattening. A detailed analysis of the band distortions induced by Hartree interaction is presented in references<sup>62,63,82,83</sup>. In this section we focus on the Hartree+U distortions. We note that the value of  $U = 4$  meV is rather large and is chosen so that Hubbard interaction induced distortions are clearly visible for all doping levels at  $\theta = 1.08^\circ$ .

The magnetic band structures for MAFM and NAFM orders are shown in Fig. 3(b) and 3(c), respectively. For both of these magnetic orders, a large gap is created at the K/K' points, owing to the sublattice symmetry breaking. For the charge neutral cases, the electronic bands are extremely flat over most of the Brillouin zone, but the effect of Hartree interactions causes the bands to distort to higher energies, as was the case without magnetic order.

For the other doping levels, the system becomes a metal, owing to partially filled dispersive bands. In each case, there remains a significant gap at the K/K' point, except at  $\nu = 3$  where only a small gap is present.

The band structures for FM order are shown in Fig. 3(d). As can be seen, at each doping level, there exist two sets of bands around the Fermi energy, which can be attributed to the spin-polarisation of the electronic states, but the valley symmetry is not broken. At charge neutrality, one set of these bands is pushed lower in energy, where the states at the edge of the Brillouin zone are lower in energy than the states near the  $\Gamma$  point. In contrast, the other set of bands around the Fermi energy at charge neutrality are pushed to higher energies, with the states at the edge of the Brillouin zone being further raised with respect to the  $\Gamma$  point. Overall, at charge neutrality, a gap exists at the Fermi energy, which means the system is a ferromagnetic insulator. These band distortions are analogous to the distortions which occur upon doping tBLG in the normal state, which is facilitated by Hartree interactions induced by adding electrons or holes. For the FM case, however, the opposite distortions occur for the spin up and spin down bands. For the other doping levels, the Hartree interactions dominate the band distortions, and the system becomes an FM metal instead of being an insulator, as there is overlap of the spin-polarised bands or/and partially filled bands.

## B. Twisted trilayer Graphene

### 1. Leading Instabilities

We now turn our attention to single twisted trilayer graphene (tTLG). This system also exhibits a magic angle, but at a twist angle of  $|\theta| = 1.54^\circ$ <sup>37</sup>. For tTLG, we follow the same procedure for our calculations as tBLG<sup>37</sup>. First we found the leading instabilities from the RPA calculations, inspected these magnetic instabilities (shown in Fig. 4), constructed appropriate approximate forms for the order parameters and performed self-consistent continuum Hartree+U calculations.

Similarly to tBLG, we find a ferromagnetic order (FM) in tTLG, as seen in Fig. 4a), which is peaked mainly on the AA regions of the inner layer<sup>37</sup>. Analogously to the bilayer, we can approximate this magnetic order with the form

$$\zeta_{FM}^{(i)} = \zeta_0^{(i)} + \zeta_1^{(i)} \sum_j \cos(\mathbf{G}_j \mathbf{r}), \quad (24)$$

where  $(i)$  is now a layer index, as the order parameters can now vary between the layers. From the symmetry of the structure, the outside layers are equivalent here, so we only need to consider the parameters to be distinct for outside vs. inside. Therefore, there are only four parameters for this magnetic order. The direction of such polarization is the same on the different sublat-

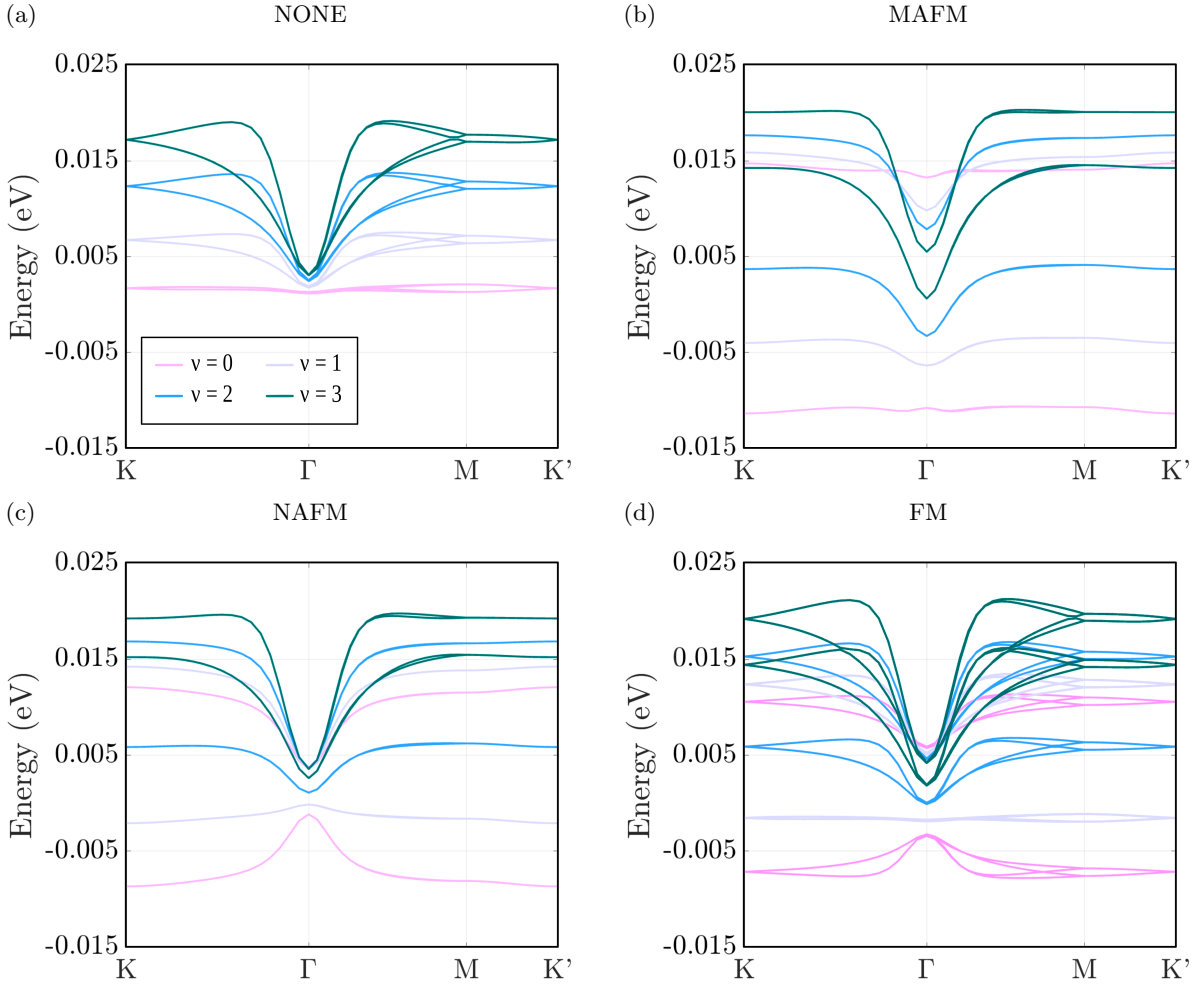


FIG. 3. The self-consistent band structures at different fillings  $\nu$  for (a): Hartree corrections only, (b): MAFM, (c): NAFM, and (d): FM. We note that a large Hubbard parameter ( $U = 4$  meV) was chosen to demonstrate the effects of gap opening on Hartree-corrected bands. Color represents different filling factors: light pink for  $\nu = 0$ ; light blue for  $\nu = 1$ ; blue for  $\nu = 2$  and dark green for  $\nu = 3$ .

tices, meaning that the sublattice-coupling  $\mathcal{S}$  is taken to be the identity matrix.

Another candidate order is the MAFM/MAFM (MMAFM) magnetic order, where both the outer and inner layers are in a moiré-scale antiferromagnetic state, as seen in Fig. 4b). This can be characterized by the following form

$$\zeta_{\text{MMAFM}}^{(i)} = \zeta_0^{(i)} + \zeta_1^{(i)} \sum_j \cos(\mathbf{G}_j \mathbf{r}). \quad (25)$$

In this case, the spin polarization in each layer is identical, and similarly to the MAFM case for tBLG, there is an opposite sign for each sublattice, meaning that  $\mathcal{S}$  is taken as the Pauli matrix  $\sigma_z$ .

With the magnetic orders from the atomistic RPA transcribed into the continuum description, we solved for the magnetic orders self-consistently and obtained the band structures self-consistently at the magic angle of  $1.54^\circ$  in tTLG. Further details of how these magnetic

orders are included in the Hamiltonian are given in the Methods section II.

## 2. Band structures

The band structure of the FM state is shown in Fig. 5(a), with the normal state band structure shown in orange for comparison. We found that this order can be stabilized with a Hubbard parameter of  $U = 1$  meV. The pair of valence and conduction flat bands in the normal state are each split into an additional pair of spin-polarized bands, giving rise to four non-degenerate flat bands in this magnetic order, similar to the observations in tBLG. The splitting between the spin-polarized valence flat bands, in other words the bottom and second-highest band, is around 1 meV at the  $\Gamma$ -point and around 2 meV at the M-point. Such splitting is suppressed at the K(K')-points. However, there is a spin-degenerate band

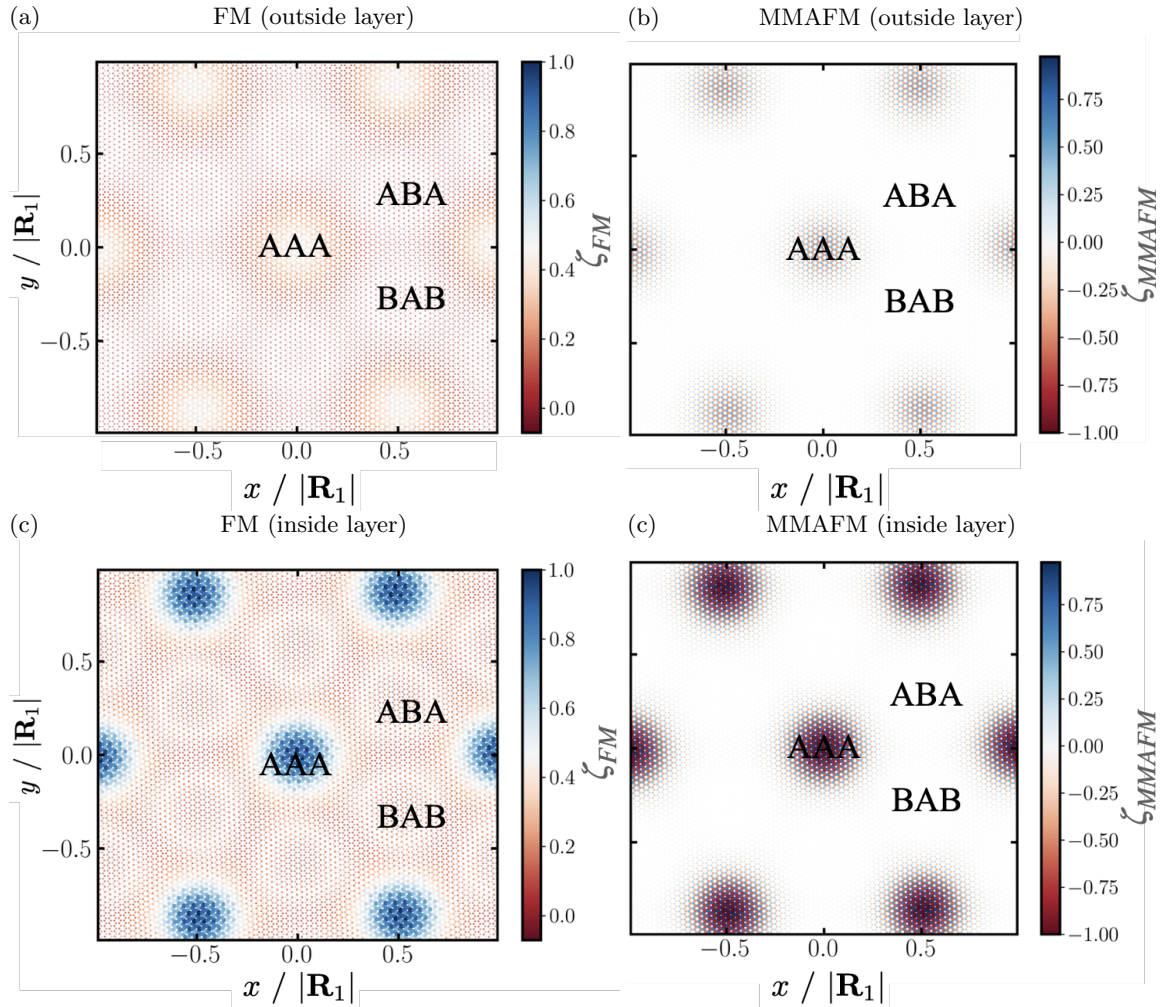


FIG. 4. Magnetic instabilities obtained from atomistic RPA calculations, which are used to incorporate magnetic forms for the continuum model. The ferromagnetic order (FM), MAFM/MAFM (MMAFM), outer-moiré antiferromagnetism (OMAFM) and MAFM/NAFM variation (MNAFM) orders are shown in a), b), c) and d), respectively. Note these plots are from the eigenvalues of these calculations, where the largest positive value was chosen to be  $\pm 1$ , and only the relevant layers are shown. These values are proportional to the spin-polarised electron density.

gap of around 3.1 meV due to time-reversal symmetry breaking in this order.

By raising the Hubbard parameter to  $U = 2$  meV, the MMAFM order can also be stabilized, which is shown in Fig. 5(b). The spin-degeneracy of bands is restored in this magnetic order, while a band gap at the K-point of around 0.93 meV persists. It does not, however, change the size of the band gaps at the  $\Gamma$ - and M-points. We found that these gaps will only further open beyond  $U = 3$  meV. It is worth noting that, for both the FM and MMAFM orders, the graphene-like Dirac cones, i.e., those with a large Fermi velocity, remain unperturbed and do not hybridize with the flat bands.

In general, for the FM and MMAFM orders, which can be stabilized with a relatively small  $U$ , the magnitude of the order parameters are around 0.1 meV. For the FM order, the constant background in all layers is approximately twice the strength of the moiré-scale os-

cillations. However, in the MMAFM order, the strengths of the constant and moiré part are almost equal in each of the layers. It is also found that the inner layer exhibits a stronger polarization than the outer layers, possibly because of the doubled moiré superlattice formed with the two outer layers, which enhances the moiré electronic effects specifically for the inner layer.

#### IV. DISCUSSION AND CONCLUSIONS

The self-consistent band structures we have obtained are consistent with those obtained by Jimeno-Pozi *et al.*<sup>78</sup> and by Klebl *et al.*<sup>75,76</sup>, who performed non-self-consistent calculations. For example, the antiferromagnetic orders which break sublattice symmetry of the graphene layers cause the Dirac cone to be destroyed, instead creating an insulating state at charge neutrality.

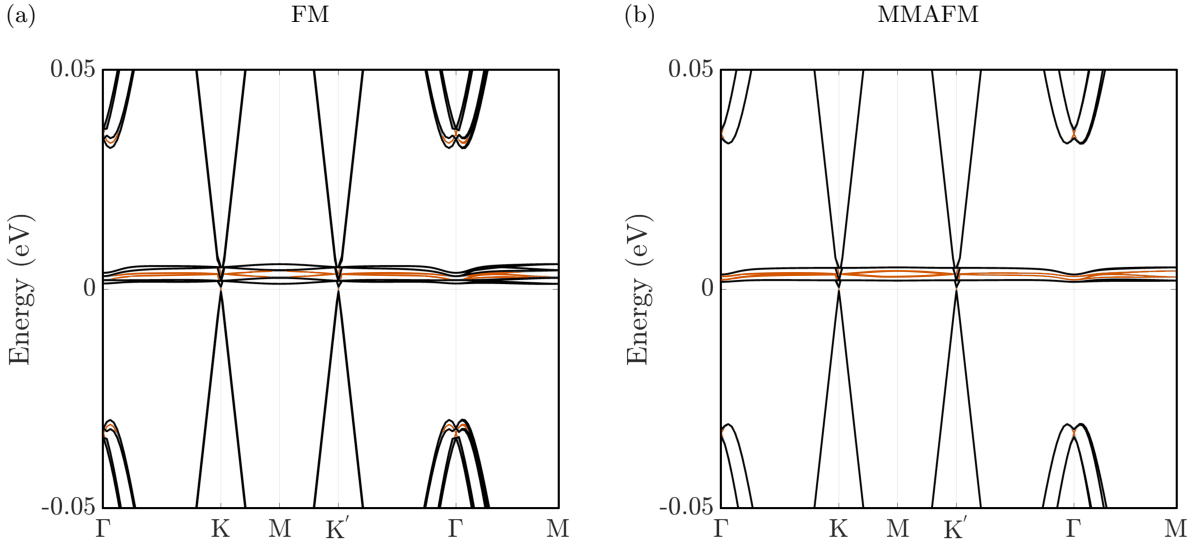


FIG. 5. Self-consistent band structures obtained of tTLG at charge neutrality at  $\theta = 1.54^\circ$  for (a) FM and (b) MMAFM. The band structure at charge neutrality without any Hubbard interactions is included in orange.

In contrast, the ferromagnetic order does not break the sublattice symmetry, but it does break the spin degeneracy, causing the bands to spin split and creating an insulating state at charge neutrality for tBLG<sup>84</sup>, which has also been observed in tTLG<sup>36</sup> for the flat bands.

While the self-consistent electronic structures obtained here qualitatively agree with those from Jimeno-Pozi *et al.*<sup>78</sup>, by inspecting the regions of stability of the three competing ground state magnetic orders, there are also a number of notable similarities comparing to the RPA predictions performed by Klelbl *et al.* in Ref. 76. According to the RPA calculations carried out in Ref. 75, the critical values of Hubbard parameter  $U_C$  reach a minimum near  $\theta = 1.08^\circ..1.05^\circ$  both with Hartree and without Hartree interactions. This indicates that tBLG is susceptible to magnetic symmetry broken phases near the magic angle. Our predicted region of stability for MAFM and NAFM is consistent with this picture, in that the largest order parameters are found near the magic angle and decay away from it. Furthermore, in the RPA calculations it was found that FM order tends to occur at the critical  $U$  for doped systems instead of M(N)AFM order. Using the continuum model in this work we also find that the M(N)AFM order parameters are suppressed for larger dopings.

As the assumed magnetic orderings here do not break any valley symmetries, creating insulating states at other doping levels than charge neutrality is not possible with the interactions included here. To go beyond this restriction, we must include longer-ranged exchange interactions, or modify the expression for the magnetic order parameters. For example, in tBLG we have constrained there to be a sum of cosines with certain polarisation on each sublattice, sometimes also including a sublattice polarised constant contribution. Instead, we could al-

low, for example, the sublattice polarisation to change in the constant and cosine contributions, allowing for more complex magnetic orderings. In the trilayer, many more instabilities were observed from the RPA calculations, and these could be included, or again more general forms of the magnetic instabilities included and self-consistently solved to find a ground state.

parameters at charge neutrality.

Overall, we have presented a formalism for the self-consistent inclusion of atomic-scale Hubbard interactions into the continuum model of moiré graphene multilayers. We have investigated this for tBLG and tTLG, for a number of magnetic instabilities, twist angles and doping levels. These developments can capture the interplay between long-ranged and short-ranged exchange interactions also in other moiré graphene multilayers, such as twisted double bilayer graphene.

## V. ACKNOWLEDGMENTS

C. T. S. C. acknowledges funding from the Croucher Foundation and an Imperial College President's Scholarship. Z.A.H.G acknowledges support through the Glasstone Research Fellowship in Materials, University of Oxford. We acknowledge the Thomas Young Centre under Grant No. TYC-101. AF and DMK acknowledge funding by the DFG within the Priority Program SPP 2244 "2DMP" – 443274199. V. V. acknowledges support from the European Union NextGenerationEU - M4, C2, Investment line 1.2 - title "Ultrafast exciton dynamics and optoelectronics in moiré superlattices - UltraDYNOMOS", CUP N. B53C24010860005. This project has received funding from the European Union's Horizon 2020 research and innovation programme un-

der the Marie Skłodowska-Curie grant agreement No. 101067977.

3.0 license at <https://github.com/VVitale/TBLG-U>.

## VI. DATA AND CODE AVAILABILITY

The data which accompanies this work will be supplied upon request. The code is freely available under a GPL-

- <sup>1</sup> Y. Cao, V. Fatemi, A. Demir, S. Fang, S. L. Tomarken, J. Y. Luo, J. D. Sanchez-Yamagishi, K. Watanabe, T. Taniguchi, E. Kaxiras, R. C. Ashoori, and P. Jarillo-Herrero, *Nature* **2018** *556*:7699 **556**, 80 (2018).
- <sup>2</sup> Y. Cao, V. Fatemi, S. Fang, K. Watanabe, T. Taniguchi, E. Kaxiras, and P. Jarillo-Herrero, *Nature* **2018** *556*:7699 **556**, 43 (2018).
- <sup>3</sup> Y. Jiang, X. Lai, K. Watanabe, T. Taniguchi, K. Haule, J. Mao, and E. Y. Andrei, *Nature* **2019** *573*:7772 **573**, 91 (2019).
- <sup>4</sup> A. L. Sharpe, E. J. Fox, A. W. Barnard, J. Finney, K. Watanabe, T. Taniguchi, M. A. Kastner, and D. Goldhaber-Gordon, *Science* **365**, 605 (2019).
- <sup>5</sup> X. Lu, P. Stepanov, W. Yang, M. Xie, M. A. Aamir, I. Das, C. Urgell, K. Watanabe, T. Taniguchi, G. Zhang, A. Bachtold, A. H. MacDonald, and D. K. Efetov, *Nature* **2019** *574*:7780 **574**, 653 (2019).
- <sup>6</sup> Y. Cao, J. Y. Luo, V. Fatemi, S. Fang, J. D. Sanchez-Yamagishi, K. Watanabe, T. Taniguchi, E. Kaxiras, and P. Jarillo-Herrero, *Physical Review Letters* **117**, 116804 (2016).
- <sup>7</sup> S. Carr, D. Massatt, S. Fang, P. Cazeaux, M. Luskin, and E. Kaxiras, *Physical Review B* **95**, 075420 (2017).
- <sup>8</sup> L. Zou, H. C. Po, A. Vishwanath, and T. Senthil, *Physical Review B* **98**, 085435 (2018).
- <sup>9</sup> Y. Choi, J. Kemmer, Y. Peng, A. Thomson, H. Arora, R. Polski, Y. Zhang, H. Ren, J. Alicea, G. Refael, F. von Oppen, K. Watanabe, T. Taniguchi, and S. Nadj-Perge, *Nature Physics* **2019** *15*:11 **15**, 1174 (2019).
- <sup>10</sup> J. Kang and O. Vafek, *Physical Review Letters* **122**, 246401 (2019).
- <sup>11</sup> A. Kerelsky, L. J. McGilly, D. M. Kennes, L. Xian, M. Yankowitz, S. Chen, K. Watanabe, T. Taniguchi, J. Hone, C. Dean, A. Rubio, and A. N. Pasupathy, *Nature* **2019** *572*:7767 **572**, 95 (2019).
- <sup>12</sup> P. Lucignano, D. Alfè, V. Cataudella, D. Ninno, and G. Cantele, *Physical Review B* **99**, 195419 (2019).
- <sup>13</sup> H. Polshyn, M. Yankowitz, S. Chen, Y. Zhang, K. Watanabe, T. Taniguchi, C. R. Dean, and A. F. Young, *Nature Physics* **2019** *15*:10 **15**, 1011 (2019).
- <sup>14</sup> Y. Xie, B. Lian, B. Jäck, X. Liu, C. L. Chiu, K. Watanabe, T. Taniguchi, B. A. Bernevig, and A. Yazdani, *Nature* **2019** *572*:7767 **572**, 101 (2019).
- <sup>15</sup> M. Yankowitz, S. Chen, H. Polshyn, Y. Zhang, K. Watanabe, T. Taniguchi, D. Graf, A. F. Young, and C. R. Dean, *Science* **363**, 1059 (2019).
- <sup>16</sup> H. Yoo, R. Engelke, S. Carr, S. Fang, K. Zhang, P. Cazeaux, S. H. Sung, R. Hovden, A. W. Tsien, T. Taniguchi, K. Watanabe, G. C. Yi, M. Kim, M. Luskin, E. B. Tadmor, E. Kaxiras, and P. Kim, *Nature Materials* **2019** *18*:5 **18**, 448 (2019).
- <sup>17</sup> E. Y. Andrei and A. H. MacDonald, *Nature Materials* **2020** *19*:12 **19**, 1265 (2020).
- <sup>18</sup> Y. Cao, D. Chowdhury, D. Rodan-Legrain, O. Rubies-Bigorda, K. Watanabe, T. Taniguchi, T. Senthil, and P. Jarillo-Herrero, *Physical Review Letters* **124**, 076801 (2020).
- <sup>19</sup> S. Carr, S. Fang, and E. Kaxiras, *Nature Reviews Materials* **2020** *5*:10 **5**, 748 (2020).
- <sup>20</sup> L. Balents, C. R. Dean, D. K. Efetov, and A. F. Young, *Nature Physics* **2020** *16*:7 **16**, 725 (2020).
- <sup>21</sup> N. Bultinck, E. Khalaf, S. Liu, S. Chatterjee, A. Vishwanath, and M. P. Zaletel, *Physical Review X* **10**, 031034 (2020).
- <sup>22</sup> K. P. Nuckolls, M. Oh, D. Wong, B. Lian, K. Watanabe, T. Taniguchi, B. A. Bernevig, and A. Yazdani, *Nature* **2020** *588*:7839 **588**, 610 (2020).
- <sup>23</sup> M. Xie and A. H. Macdonald, *Physical Review Letters* **124**, 097601 (2020).
- <sup>24</sup> Y. Zhang, K. Jiang, Z. Wang, and F. Zhang, *Physical Review B* **102**, 035136 (2020).
- <sup>25</sup> U. Zondiner, A. Rozen, D. Rodan-Legrain, Y. Cao, R. Queiroz, T. Taniguchi, K. Watanabe, Y. Oreg, F. von Oppen, A. Stern, E. Berg, P. Jarillo-Herrero, and S. Ilani, *Nature* **2020** *582*:7811 **582**, 203 (2020).
- <sup>26</sup> Y. Cao, D. Rodan-Legrain, J. M. Park, N. F. Yuan, K. Watanabe, T. Taniguchi, R. M. Fernandes, L. Fu, and P. Jarillo-Herrero, *Science* **372**, 264 (2021).
- <sup>27</sup> Y. Choi, H. Kim, C. Lewandowski, Y. Peng, A. Thomson, R. Polski, Y. Zhang, K. Watanabe, T. Taniguchi, J. Alicea, and S. Nadj-Perge, *Nature Physics* **2021** *17*:12 **17**, 1375 (2021).
- <sup>28</sup> I. Das, X. Lu, J. Herzog-Arbeitman, Z. D. Song, K. Watanabe, T. Taniguchi, B. A. Bernevig, and D. K. Efetov, *Nature Physics* **2021** *17*:6 **17**, 710 (2021).
- <sup>29</sup> J. Liu and X. Dai, *Physical Review B* **103**, 035427 (2021).
- <sup>30</sup> D. M. Kennes, M. Claassen, L. Xian, A. Georges, A. J. Millis, J. Hone, C. R. Dean, D. N. Basov, A. N. Pasupathy, and A. Rubio, *Nature Physics* **2021** *17*:2 **17**, 155 (2021).
- <sup>31</sup> A. Rozen, J. M. Park, U. Zondiner, Y. Cao, D. Rodan-Legrain, T. Taniguchi, K. Watanabe, Y. Oreg, A. Stern, E. Berg, P. Jarillo-Herrero, and S. Ilani, *Nature* **2021** *592*:7853 **592**, 214 (2021).
- <sup>32</sup> Y. Saito, F. Yang, J. Ge, X. Liu, T. Taniguchi, K. Watanabe, J. I. Li, E. Berg, and A. F. Young, *Nature* **2021** *592*:7853 **592**, 220 (2021).
- <sup>33</sup> M. Oh, K. P. Nuckolls, D. Wong, R. L. Lee, X. Liu, K. Watanabe, T. Taniguchi, and A. Yazdani, *Nature* **2021** *600*:7888 **600**, 240 (2021).
- <sup>34</sup> S. Wu, Z. Zhang, K. Watanabe, T. Taniguchi, and E. Y. Andrei, *Nature Materials* **2021** *20*:4 **20**, 488 (2021).

- <sup>35</sup> Y. Xie, A. T. Pierce, J. M. Park, D. E. Parker, E. Khalaf, P. Ledwith, Y. Cao, S. H. Lee, S. Chen, P. R. Forrester, K. Watanabe, T. Taniguchi, A. Vishwanath, P. Jarillo-Herrero, and A. Yacoby, *Nature* **2021** *600*:7889 **600**, 439 (2021).
- <sup>36</sup> Z. Hao, A. M. Zimmerman, P. Ledwith, E. Khalaf, D. H. Najafabadi, K. Watanabe, T. Taniguchi, A. Vishwanath, and P. Kim, *Science* **371**, 1133 (2021).
- <sup>37</sup> A. Fischer, Z. A. Goodwin, A. A. Mostofi, J. Lischner, D. M. Kennes, and L. Klebl, *npj Quantum Materials* **2022** *7*:1 **7**, 1 (2022).
- <sup>38</sup> C. Zhang, T. Zhu, S. Kahn, S. Li, B. Yang, C. Herbig, X. Wu, H. Li, K. Watanabe, T. Taniguchi, S. Cabrini, A. Zettl, M. P. Zaletel, F. Wang, and M. F. Crommie, *Nat. Commun.* **2021**, 2516 (12).
- <sup>39</sup> C. Rubio-Verdú, S. Turkel, L. Song, L. Klebl, R. Samajdar, M. S. Scheurer, J. W. F. Venderbos, K. Watanabe, T. Taniguchi, H. Ochoa, L. Xian, D. Kennes, R. M. Fernandes, A. Rubio, and A. N. Pasupathy, *Nat. Phys.*, <https://doi.org/10.1038/s41567> (2021).
- <sup>40</sup> M. He, Y. Li, J. Cai, Y. Liu, K. Watanabe, T. Taniguchi, X. Xu, and M. Yankowitz, *Nat. Phys.* **17**, 26–30 (2021).
- <sup>41</sup> X. Liu, Z. Hao, E. Khalaf, J. Y. Lee, K. Watanabe, T. Taniguchi, A. Vishwanath, and P. Kim, *Nature* **583**, 221 (2020).
- <sup>42</sup> Z. A. H. Goodwin, L. Klebl, V. Vitale, X. Liang, V. Gogtay, X. van Gorp, D. M. Kennes, A. A. Mostofi, and J. Lischner, *Phys. Rev. Materials* **5**, 084008 (2021).
- <sup>43</sup> A. M. Seiler, F. R. Geisenhof, F. Winterer, K. Watanabe, T. Taniguchi, T. Xu, F. Zhang, and R. T. Weitz, *Nature* **608**, 298 (2022).
- <sup>44</sup> H. Zhou, T. Xie, T. Taniguchi, K. Watanabe, and A. F. Young, *Nature* **598**, 434 (2021).
- <sup>45</sup> H. Zhou, L. Holleis, Y. Saito, L. Cohen, W. Huynh, C. L. Patterson, F. Yang, T. Taniguchi, K. Watanabe, and A. F. Young, *Science* **375**, 774 (2022).
- <sup>46</sup> Y. Zhang, R. Polski, A. Thomson, É. Lantagne-Hurtubise, C. Lewandowski, H. Zhou, K. Watanabe, T. Taniguchi, J. Alicea, and S. Nadj-Perge, *Nature* **613**, 268 (2023).
- <sup>47</sup> Y.-C. Tsui, M. He, Y. Hu, E. Lake, T. Wang, K. Watanabe, T. Taniguchi, M. P. Zaletel, and A. Yazdani, *Nature* **628**, 287 (2024).
- <sup>48</sup> T. Han, Z. Lu, Y. Yao, L. Shi, J. Yang, J. Seo, S. Ye, Z. Wu, M. Zhou, H. Liu, G. Shi, Z. Hua, K. Watanabe, T. Taniguchi, P. Xiong, L. Fu, and L. Ju, “Signatures of chiral superconductivity in rhombohedral graphene,” (2024), arXiv:2408.15233 [cond-mat.mes-hall].
- <sup>49</sup> Z. Lu, T. Han, Y. Yao, A. P. Reddy, J. Yang, J. Seo, K. Watanabe, T. Taniguchi, L. Fu, and L. Ju, *Nature* **626**, 759 (2024).
- <sup>50</sup> A. M. Valerio Vitale, Kemal Atalar and J. Lischner, *2D Materials* (2022).
- <sup>51</sup> M. H. Naik and M. Jain, *Phys. Rev. Lett.* **121**, 266401 (2018).
- <sup>52</sup> F. Wu, T. Lovorn, E. Tutuc, I. Martin, and A. H. MacDonald, *Phys. Rev. Lett.* **122**, 086402 (2019).
- <sup>53</sup> Y. Xia, Z. Han, K. Watanabe, T. Taniguchi, J. Shan, and K. F. Mak, *Nature* **637**, 833 (2025).
- <sup>54</sup> Y. Guo, J. Pack, J. Swann, L. Holtzman, M. Cothrine, K. Watanabe, T. Taniguchi, D. G. Mandrus, K. Barmak, J. Hone, *et al.*, *Nature* **637**, 839 (2025).
- <sup>55</sup> H. Park, J. Cai, E. Anderson, Y. Zhang, J. Zhu, X. Liu, C. Wang, W. Holtzmann, C. Hu, Z. Liu, *et al.*, *Nature* **622**, 74 (2023).
- <sup>56</sup> Z. A. H. Goodwin and V. Fal’ko, *J. Phys.: Condens Matter* (2022).
- <sup>57</sup> A. M. Christopher Cheung, Zachary A H Goodwin and J. Lischner, *Nano Lett.* (2024).
- <sup>58</sup> L. Xian, D. M. Kennes, N. Tancogne-Dejean, M. Altarelli, and A. Rubio, *Nano Letters* **19**, 4934 (2019).
- <sup>59</sup> N. R. Walet and F. Guinea, *Phys. Rev. B* **103**, 125427 (2021).
- <sup>60</sup> R. Bistritzer and A. H. MacDonald, *Proceedings of the National Academy of Sciences of the United States of America* **108**, 12233 (2011).
- <sup>61</sup> F. Guinea and N. R. Walet, *Proceedings of the National Academy of Sciences of the United States of America* **115**, 13174 (2018).
- <sup>62</sup> T. Cea, N. R. Walet, and F. Guinea, *Physical Review B* **100**, 205113 (2019).
- <sup>63</sup> T. Cea and F. Guinea, *Physical Review B* **102**, 045107 (2020).
- <sup>64</sup> T. Cea, P. A. Pantaleón, N. R. Walet, and F. Guinea, *Nano Materials Science* **4**, 27 (2022).
- <sup>65</sup> M. Xie and A. H. MacDonald, *Phys. Rev. Lett.* **124**, 097601 (2020).
- <sup>66</sup> J. Kang and O. Vafek, *Phys. Rev. X* **8**, 031088 (2018).
- <sup>67</sup> M. Koshino, N. F. Q. Yuan, T. Koretsune, M. Ochi, K. Kuroki, and L. Fu, *Phys. Rev. X* **8**, 031087 (2018).
- <sup>68</sup> Z. A. H. Goodwin, V. Vitale, F. Corsetti, D. Efetov, A. A. Mostofi, and J. Lischner, *Phys. Rev. B* **101**, 165110 (2020).
- <sup>69</sup> Z. A. H. Goodwin, F. Corsetti, A. A. Mostofi, and J. Lischner, *Phys. Rev. B* **100**, 121106(R) (2019).
- <sup>70</sup> Z. A. H. Goodwin, F. Corsetti, A. A. Mostofi, and J. Lischner, *Phys. Rev. B* **100**, 235424 (2019).
- <sup>71</sup> L. A. Gonzalez-Arraga, J. L. Lado, F. Guinea, and P. San-Jose, *Physical Review Letters* **119**, 107201 (2017).
- <sup>72</sup> A. Lopez-Bezanilla, *Phys. Rev. Materials* **3**, 054003 (2019).
- <sup>73</sup> J. González and T. Stauber, *Phys. Rev. B* **104**, 115110 (2021).
- <sup>74</sup> J. Vahedi, R. Peters, A. Missaoui, A. Honecker, and G. T. de Laissardiére, *SciPost Phys.* **11**, 083 (2021).
- <sup>75</sup> L. Klebl and C. Honerkamp, *Physical Review B* **100**, 155145 (2019).
- <sup>76</sup> L. Klebl, Z. A. Goodwin, A. A. Mostofi, D. M. Kennes, and J. Lischner, *Physical Review B* **103**, 195127 (2021).
- <sup>77</sup> A. Fischer, L. Klebl, C. Honerkamp, and D. M. Kennes, *Physical Review B* **103**, L041103 (2021).
- <sup>78</sup> A. Jimeno-Pozo, Z. A. H. Goodwin, P. A. Pantaleón, V. Vitale, L. Klebl, D. M. Kennes, A. A. Mostofi, J. Lischner, and F. Guinea, *Adv. Phys. Res.* **2**, 2300048 (2023).
- <sup>79</sup> T. Cea and F. Guinea, *Phys. Rev. B* **102**, 045107 (2020).
- <sup>80</sup> T. Cea, N. R. Walet, and F. Guinea, *Phys. Rev. B* **100**, 205113 (2019).
- <sup>81</sup> Z. A. H. Goodwin, V. Vitale, X. Liang, A. A. Mostofi, and J. Lischner, *Electron. Struct.* **2**, 034001 (2020).
- <sup>82</sup> T. Cea and F. Guinea, *Proceedings of the National Academy of Sciences of the United States of America* **118**, e2107874118 (2021).
- <sup>83</sup> Z. A. Goodwin, V. Vitale, X. Liang, A. A. Mostofi, and J. Lischner, *Electronic Structure* **2**, 034001 (2020).
- <sup>84</sup> X. Lu, P. Stepanov, W. Yang, M. Xie, M. A. Aamir, I. Das, C. Urgell, K. Watanabe, T. Taniguchi, G. Zhang, A. Bachtold, A. H. MacDonald, and D. K. Efetov, *Nature* **574**, 653–657 (2019).